Magnetoelectric interaction and transport behaviors in magnetic nanocomposite thermoelectric materials under the intrinsic excitation

Wenyu Zhao[1], Zhiyuan Liu[1], Ping Wei[1], Qingjie Zhang[1, *], Wanting Zhu[1], Xianli Su[1], Xinfeng Tang[1], Jihui Yang[2,*], Yong Liu[3], Jing Shi[3], Yimin Chao[4], Siqi Lin[5], and Yanzhong Pei[5]

How to suppress the performance deterioration of thermoelectric materials in the intrinsic excitation region remains a key challenge. The magnetic transition of permanent magnet nanoparticles from ferromagnetism to paramagnetism provides an effective approach for the solution of this challenge. Here we have designed and prepared the magnetic nanocomposite thermoelectric materials consisting of $BaFe_{12}O_{19}$ nanoparticles (BaM-NPs) and $Ba_{0.3}In_{0.3}Co_4Sb_{12}$ matrix. It is discovered that the electrical transport behaviors of the nanocomposites have been controlled by the magnetic transition of BaM-NPs from ferromagnetism to paramagnetism. BaM-NPs trap the elctrons below the Curie temperature (T_C) and release the trapped electrons above the T_C, playing an "electron repository" role in maintaining high ZT. BaM-NPs produce two types of magnetoelectric effects of electron spiral motion and magnon-drag thermopower besides enhancing phonon scattering. Our work demonstrates that the thermoelectric performance deterioration in the intrinsic excitation region can be suppressed through the magnetic transition of permanent magnet nanoparticles.

Thermoelectric (TE) materials have attracted much interest owing to the fascinating applications in recycling utilization of industrial waste heat and automobile exhaust heat, high-efficiency cooling of next-generation integrated circuits, and full-spectrum solar power generation[1,2]. The properties of TE materials are characterized by dimensionless figure of merit $ZT=\alpha^2\sigma T/(\kappa_E+\kappa_L)$. Where T, α, σ, κ_E and κ_L are the absolute temperature, Seebeck coefficient, electrical conductivity, and the electronic and lattice components of the thermal conductivity (κ), respectively. To optimize the thermal properties, various phonon engineering approaches were used to enhance phonon scattering and decrease κ_L by having taken advantage of nanoinclusion[3-13]. A series of band structure engineering approaches were employed to improve the electrical properties[14-20]. Recently, we discovered that the electrical and thermal properties of TE materials could be simultaneously optimized through coexisting multi-localization transport behavior[21]. However, TE materials have been facing a serious problem that the intrinsic excitation unavoidably results in the deterioration of high-temperature performance. Up to now, it remains a key challenge how to suppress the performance deterioration of TE materials in the intrinsic excitation region.

Based on the Maxwell's electromagnetic theory, the charged particles (electrons and holes) are confined to circular paths or helixes and even trapped by magnetic impurities owing to the Lorentz force ($\boldsymbol{F}_L$)[22]. To achieve excellent electrical transport properties, all semiconductor materials including various TE materials had been generally required to eliminate the magnetic impurities in the past decades. This understanding has limited the development of magnetic nanocomposite TE materials. Here we propose an idea of using magnetic transition of permanent magnet nanoparticles from ferromagnetism to paramagnetism to suppress the performance deterioration of TE materials in the intrinsic excitation region. We choose filled $CoSb_3$ as TE matrix and M-type barium ferrite $BaFe_{12}O_{19}$ nanoparticles (BaM-NPs) as permanent magnet inclusions to prepare a series of magnetic nanocomposite TE materials. Filled $CoSb_3$ has excellent high-temperature stability and is an important lead-free TE material for intermediate temperature power generation[8,23-31]. M-type barium ferrite, $BaFe_{12}O_{19}$ (BaM), is an important permanent magnet owing to the strong magnetic anisotropy, high Curie temperature (T_C), and large coercive force (H_C). Using nanostructuring approaches we can adjust the T_C of BaM from 726 K for the bulk materials[32] close to the intrinsic excitation temperature of filled $CoSb_3$ and improve the H_C beneficial to trapping more electrons.

Structure characterization

The xBaM/$Ba_{0.3}In_{0.3}Co_4Sb_{12}$ magnetic nanocomposite TE materials we studied contain BaM-NPs with weight percentage x=0, 0.15%, 0.25%, 0.35% and 0.45%, labeled as MNC00 ($Ba_{0.3}In_{0.3}Co_4Sb_{12}$ matrix), MNC15, MNC25, MNC35, and MNC45. All the XRD diffraction peaks of xBaM/$Ba_{0.3}In_{0.3}Co_4Sb_{12}$ can be indexed to those of $CoSb_3$ (**Figure S1**), indicating that the matrix remains good chemical stability in the presence of BaM-NPs. The diffraction peaks of BaM were not detected because the highest content of BaM-NPs is only 0.45% and far less than the detection limit of XRD technique (about 1%). The grain boundaries and interfaces are straight and very clean without any impurity particles in the matrix, as shown in **Figure 1a**. However, BaM-NPs with 20~150 nm in size were randomly distributed on the interfaces and boundaries of the matrix, as examplied by MNC45 (**Figure 1b**). In particular, some BaM-NPs with less than 10 nm in size were pinned into the $Ba_{0.3}In_{0.3}Co_4Sb_{12}$ grains (**Figure 1c**). The rough interfaces and boundaries

---

[1] State Key Laboratory of Advanced Technology for Materials Synthesis and Processing, Wuhan University of Technology, Wuhan 430070, China.
[2] Department of Materials Science and Engineering, University of Washington, Seattle, WA 98195, USA.
[3] School of Physics and Technology, Wuhan University, Wuhan 430072, China.
[4] Energy Materials Laboratory, School of Chemistry, University of East Anglia, Norwich Research Park NR4 7TJ, UK.
[5] School of Materials Science and Engineering, Tongji University, Shanghai 200092, China
Correspondence and requests for materials should be addressed to Q.-J. Z. (zhangqj@whut.edu.cn) and J.-H. Y. (jihuiy@uw.edu).

induced by BaM-NPs are beneficial to enhancing the phonon scattering.

XPS of Sb $3d_{5/2}$ and $3d_{3/2}$ core levels for the matrix are composed of double peaks (**Figure S2**), a similar phenomenon was observed in our previous work[31]. The peaks of Sb $3d_{5/2}$ and $3d_{3/2}$ core levels of xBaM/$Ba_{0.3}In_{0.3}Co_4Sb_{12}$ have no any chemical shift as compared with those of the matrix, suggesting that BaM-NPs did not affect the electron structure of the matrix. Based on the reported Raman results[33], four recognizable Raman peaks of xBaM/$Ba_{0.3}In_{0.3}Co_4Sb_{12}$ are almost the same as that of the matrix (**Figure S3**), indicating that BaM-NPs do not affect the symmetry of the Sb_4 rings in the matrix. These structural features confirm that BaM-NPs did not enter into the lattice of the matrix and act as secondary-phase impurity.

Electrical and thermal transport properties

The temperature dependences of R_H, n and μ_H in the range of 300-775K (**Figure 2**) indicates that the majority carriers of the matrix and xBaM/$Ba_{0.3}In_{0.3}Co_4Sb_{12}$ are electrons, exhibiting n-type conduction behavior. The temperature dependence of R_H of the matrix is very similar to that of p-type $CoSb_3$[34] and $Mg_xPb_{1-x}Te$[35], indicating the validity of the high temperature Hall measurement in the present study. The R_H increases slightly and the n decreases correspondingly with increasing temperature from 550 K to 650 K. The abnormal temperature dependences of R_H and n for the matrix may be explained as a result of the decrease of the electron concentration in the downmost conduction band due to the excitation of electrons from it to the second conduction band, as pointed out in **Ref. 36**. The decreases in R_H and μ_H and the increase in n above 675 K are attributed to the intrinsic excitation of the matrix. The absolute values of R_H for all xBaM/$Ba_{0.3}In_{0.3}Co_4Sb_{12}$ increased while the μ_H and n reduced as compared with those of the matrix in the low temperature range below 575-650 K. These results show that BaM-NPs lower the n below 575-650 K. However, the R_H and μ_H rapidly decreased while the n rapidly increased with increasing the temperature above 575-650 K. Note that the variations of R_H, n and μ_H gradually increased as the x increased above 575-650 K because of the presence of BaM-NPs. Here, it needs a reasonable explanation why BaM-NPs in xBaM/$Ba_{0.3}In_{0.3}Co_4Sb_{12}$ can lower the n in the low temperature range and remarkably impact the R_H, n and μ_H in the high temperature range.

The temperature dependences of σ and α in the range of 300-850 K (**Figure 3a and 3b**) show that the intrinsic excitation temperature of the matrix is about 675 K. For xBaM/$Ba_{0.3}In_{0.3}Co_4Sb_{12}$, the σ decreased and the α increased with increasing the x in the range of 0.15~0.35%. The similar temperature dependences of σ and α of MNC15 indicate that the electrical transport properties above 675 K are mainly affected by the intrinsic excitation of the matrix. However, different from MNC15, for the samples with $x \geq 0.25\%$ the σ modestly reduced while the α continuously increased in the range of 675-850 K. Here also needs a reasonable explanation for the different temperature dependences of σ and α induced by BaM-NPs above 675 K. The significant decreases in σ and α of MNC45 indicate that the optimal content of BaM-NPs should be about 0.35%. As shown in the inset of **Figure 3b**, the power factor ($\alpha^2\sigma$) of MNC35 is much higher than that of the matrix in the whole range of 300-850 K. The largest $\alpha^2\sigma$ reached 4.48 $mW \cdot m^{-1} \cdot K^{-2}$ at 700 K. It is worth noting that the $\alpha^2\sigma$ of MNC35 remains almost unchanged in the range of 675-850 K. The temperature dependences of α of MNC00 and MNC35 in the range of 90-300 K under zero field and an applied magnetic field of 0.4 T (**Figure S4**) also confirm that the BaM-NPs can significantly increase the α of xBaM/$Ba_{0.3}In_{0.3}Co_4Sb_{12}$.

As shown in **Figure 3c**, the κ of xBaM/$Ba_{0.3}In_{0.3}Co_4Sb_{12}$ significantly reduced as compared with that of the matrix, indicating that BaM-NPs can effectively improve the thermal properties. The κ_E of xBaM/$Ba_{0.3}In_{0.3}Co_4Sb_{12}$ gradually increased as the temperature rose in the range of 300-675 K, which originated from the electron contribution. However, above 675 K the κ_E first rapidly increased, then slowly increased, and last slightly decreased with increasing the x in the range of 0.15~0.45%, as shown in **Figure 3d**. The κ_L values of xBaM/$Ba_{0.3}In_{0.3}Co_4Sb_{12}$ with $x \geq 0.25\%$ are much less than those of the matrix in the range of 300-675 K as shown in **Figure 3e**, which is attributed to the enhanced interface scattering induced by BaM-NPs. The lowest κ_L is only 0.7 $W \cdot m^{-1} \cdot K^{-1}$ at 675 K for MNC35. The rapid reduction in κ_L for all the samples with increasing the temperature in the range of 300-675 K is owing to the enhanced lattice vibration. The temperature dependence of κ_L for all the samples in the range of 300-675 K is close to T^{1}, indicating that the phonon-phonon Umklapp scattering is dominant[37]. The slow decrease in the κ_L below 675 K originates from the compromise between the bipolar thermal diffusion and the enhanced phonon scattering. The slight increase in the κ_L above 675 K indicats that the thermal transport of the nanocomposites is dominated by the bipolar thermal diffusion in the intrinsic excitation region.

The ZT values of xBaM/$Ba_{0.3}In_{0.3}Co_4Sb_{12}$ in the range of 300-850 K first increased in the x range of 0-0.35% and then decreased when $x > 0.35\%$, as shown in **Figure 3f**. The largest ZT reached 1.64 at 850 K for MNC35, increased by 22% as compared with that of the matrix. It is worth noting that the average ZT is more than 1.52 in the range of 675-850 K, indicating that BaM-NPs can maintain high ZT values in the intrinsic excitation region. Particularly, unlike the usual situation[29,30], where the majority of the enhancement in ZT is the reduction of the κ_L, in our present work, it is the significant reduction in the κ_E, associated with the reduced σ, because of almost the same κ_L of MNC35 and MNC00 (**Table SI**). In addition, the α is increased by about 12 % which is consistent with the decrease of σ.

Magnetoelectric interaction and its beneficial roles

The hysteresis loops of BaM-NPs, MNC00, and MNC45 (**Figure S5**) reveal that the nanocomposites have ferromagnetism. The remnant magnetization (M_r) and H_C of BaM-NPs are about 6.9 emu/g and 2218 Oe, respectively. The H_C is much higher than that of micron-sized BaM about 400 Oe[38], beneficial to trapping more electrons below the T_C. The matrix shows very weak ferromagnetism due to Fe impurity from iron can and hammer used during the sample process, because $Ba_{0.44}Co_4Sb_{12}$ revealed paramagnetism at room temperature[39]. The M_r and H_C of MNC45 are remarkably greater than those of the matrix but much lower than those of BaM-NPs, which are about 9.7×10^{-4} emu/g and 136 Oe, respectively. The negative differential magnetization in both the matrix and MNC45 under high magnetic field revealed a typical feature of field-induced antiferromagnetic coupling, as reported in discontinuous Ni nanoparticles in Al matrix[40].

Theoretically, since the c axis of BaM is the easy magnetization direction, an effective magnetocrystalline anisotropy field (H_A) parallel to the c axis is generated in BaM-NPs (**Figure S6a**). In xBaM/$Ba_{0.3}In_{0.3}Co_4Sb_{12}$, the majority carriers (electrons) and magnons will drift from the hot side (T_H), to the cold side (T_L) as driven by thermal energy. There are at leat three kinds of electrons with velocities v_1, v_2 and v_3 in xBaM/$Ba_{0.3}In_{0.3}Co_4Sb_{12}$, which are parallel to, perpendicular to, and components parallel and perpendicular to the H_A (**Figure S6b**). Therefore, based on our understanding about the effects of permanent magnet nanoparticles on electrical transport behavior of TE materials (**Figure S7**), the electrons with v_1 move linearly and are not affected by the H_A, the electrons with v_2 are confined to circular paths, and the electrons with v_3 move in a spiral pattern and are trapped by BaM-NPs. The spiral motion may reasonably explain why BaM-NPs can lower the n of xBaM/$Ba_{0.3}In_{0.3}Co_4Sb_{12}$ in the low temperature range. As a result, the reduction in the n at room temperature from 4.9×10^{20} cm^{-3} for the matrix to 3.8×10^{20} cm^{-3} for the MNC15 sample is attributed to the electron trapping effect of the H_A induced by BaM-NPs. However, like all the permanent magnets, BaM-NPs must undergo a magnetic transition from ferromagnetism to paramagnetism when the working temperature (T_W) is higher than the T_C. BaM-NPs are in the ferromagnetism state and produce a nonuniform spherical magnetic field when $T_W<T_C$, trapping the electrons owing to the spiral motion. The nonuniform spherical magetric field will disappear and BaM-NPs are in the paramagnetism state when $T_W>T_C$, releasing the trapped electrons. The "electron repository" role of BaM-NPs has been experimentally confirmed by the significant increase in the n of xBaM/$Ba_{0.3}In_{0.3}Co_4Sb_{12}$ above 675 K (**Figure 2b**). Based on the temperature dependences of magnetization of BaM-NPs (**Figure 4**), the T_C of BaM-NPs is about 669 K under 0.6 T and 673 K under 2.0 T, which is very close to the intrinsic excitation temperature of the matrix (about 675 K). Therefore, we firmly believe that the magnetic transition of BaM-NPs from ferromagnetism to paramagnetism must occur in xBaM/$Ba_{0.3}In_{0.3}Co_4Sb_{12}$ near 675 K, and that the electrical transport behaviors in the intrinsic excitation region must have been controlled by the magnetic transition. Especially, all the abnormal changes in R_H, n, μ_H, σ, α, κ_L and κ_E of xBaM/$Ba_{0.3}In_{0.3}Co_4Sb_{12}$ above 675 K may be reasonably explained with the magnetic transition.

Compared with the matrix, besides electron-phonon interaction, there must exist electron-magnon interaction in xBaM/$Ba_{0.3}In_{0.3}Co_4Sb_{12}$. Namely, the magnon-drag effect must occur and produce an extra thermopower (S_m) in the nanocomposties, similar to that in FeNi nanowires[41] and NiCu alloy[42]. Therefore, the measured α of xBaM/$Ba_{0.3}In_{0.3}Co_4Sb_{12}$ is the sum of S from Seebeck effect and S_m from magnon-drag effect. The magnon-drag effect may reasonably explain why BaM-NPs can cause the significant increase in α of the nanocomposties. The understanding has been supported by the experimental results (**Figure 2** and **Figure S4**).

Figure 5 displays the temperature dependences of σ and α of magnetized MNC00 and magnetized MNC35 in the range of 300-850 K. The samples magnetized along the A, B and C directions are labeled as A_MNC00, B_MNC00, C_MNC00, A_MNC35, B_MNC35, C_MNC35 (**Figure S8**). After magnetization, the σ of MNC00 kept almost unchanged in the range of 300-675 K and significantly decreased above 675 K while the α was almost unchanged in the range of 300-850 K. The different temperature dependences of σ for the MNC00 before and after magnetization suggest that the remanence was preserved in the magnetized MNC00, in good agreement with the magnetic measurement result. It is worth noting that for the magnetized MNC35 the σ and α have no obvious change in the range of 300-675 K and are almost unchanged above 675 K, however, for the unmagnetized MNC35 the σ and α simultaneously decreased above 675 K. Obviously, after magnetization the discrepancy between MNC00 and MNC35 must originate from the presence of BaM-NPs. These results indicate that the applied magnetic field of 0.2 T has no effect on the σ and α of MNC35 in the range of 300-675 K. The phenomenon was also observed in the range of 90-300 K where an applied magnetic field of 0.4 T had no effect on the α (**Figure S4**). It is easy to understand that below the T_C the applied magnetic field does not affect the electrical transport of xBaM/$Ba_{0.3}In_{0.3}Co_4Sb_{12}$, because BaM-NPs are in the ferromagnetic state in the range of 90-675 K.

Figure S9 show the effect of disappearance of the H_A on the TE properties of xBaM/$Ba_{0.3}In_{0.3}Co_4Sb_{12}$ above 675 K and the mechanism of magnetoelectric interaction in MNC00 and MNC35 before and after magnetization. An effective magnetic field (H_p) parallel to the applied magnetic field will occur in the magnetized MNC00. The H_A induced by BaM-NPs are randomly oriented in the unmagnetized MNC35, however, the randomly oriented H_A had been rearranged and were parallel to the applied magnetic field in the magnetized MNC35. Obviously, the magnetic field strength of the H_A induced by BaM-NPs are much greater than that of the H_p from the matrix. The detailed mechanism that the H_A and H_p control the electron motion see Supplementary information section. The discrepancy in the temperature dependences of σ and α of magnetized MNC00 and magnetized MNC35 above 675 K as shown in **Figure 3a-b** may be attributed to the different strength between the H_p and H_A. The strong H_A can not only produce magnetoelectric effects of electron spiral motion and magnon-drag thermopower, but also trap the electrons; however, the weak H_p can only produce the weak magnetoelectric effects. Therefore, the disappearance of H_p at high temperature doesn't produce extra electrons except for the disappearance of magnetoelectric effects. This is the reason why for the magnetized MNC00, the α remains almost unchanged but the σ decreases, as compared to that of the un-magnetized MNC00 above 675 K. On the contrary, the disappearance of the H_A must change the carrier concentration because those electrons trapped by BaM-NPs will become conduction electrons again according to the temperature dependence of the n of xBaM/$Ba_{0.3}In_{0.3}Co_4Sb_{12}$ above 675 K as shown in **Figure 2b**. It is easy to understand that the extra conduction electrons can suppress the negative impacts of minority carriers (holes) from the intrinsic excitation of the matrix on the majority carriers, and compensate for the decrease in the n induced by the enhanced carriers scattering at high temperature. The magnetic field strength discrepancy between H_A and H_p can reasonably explain why above 675 K the σ and α of magnetized MNC35 remain almost unchanged and why the α of magnetized MNC00 remains almost unchanged but the σ decreases.

For xBaM/$Ba_{0.3}In_{0.3}Co_4Sb_{12}$, the σ decreased rather than increased above the T_C before magnetization (**Figure 3a**), indicating that the influence of the decreased μ_H is larger than that of the increased n according to the relation $\sigma=ne\mu$. There are at least three kinds of scattering mechanisms above the T_C to cause the reduction of μ_H in the nanocomposites as follows: (1) spin disorder scattering due to the magnetic transition of BaM-NPs from ordered ferromagnetic state to disordered paramagnetic state, (2) electron-hole scattering induced by the intrinsic exaction of the matrix[43], and (3) electron-phonon scattering. Therefore, the discrepancy in the σ of MNC35 before and after magnetization (**Figure 3a** and **Figure 5a**) is attributed to the more electrons being trapped by BaM-NPs after magnetization than the case before magnetization. At the same time, the magnetic transition of BaM-NPs from ferromagnetism to paramagnetism must also affect the thermal transport properties, because the magnon-phonon, magnon-electron, and electron-phonon interactions must be changed. The abnormal increase in the κ_L above 675 K should originate from the disappearance of the H_A. The x dependence of κ_E (**Figure 3d**) is beneficial to decreasing the κ above 675 K and have been also reasonably explained with the disappearance of the H_A. As a result, the κ is largely lowered for MNC35 and a high average ZT is maintained at high temperatures.

References

1. Bell, L. E. Cooling, heating, generating power, and recovering waste heat with thermoelectric systems. *Science* **321**, 1457–1461 (2008).
2. Snyder, G. J. & Toberer, E. S. Complex thermoelectric materials. *Nature Mater.* **7**, 105–114 (2008).
3. Biswas, K. *et al.* High-performance bulk thermoelectrics with all-scale hierarchical architectures. *Nature* **489**, 414–418 (2012).
4. Hsu, K. F. *et al.* Cubic $AgPb_mSbTe_{2+m}$: Bulk thermoelectric materials with high figure of merit. *Science* **303**, 818–821 (2004).
5. Dresselhaus, M. S. *et al.* New directions for low-dimensional thermoelectric materials. *Adv. Mater.* **19**, 1043–1053 (2007).
6. Poudel, B. *et al.* High-thermoelectric performance of nanostructured bismuth antimony telluride bulk alloys. *Science* **320**, 634–638 (2008).
7. Zhu T. *et al.* High efficiency half-Heusler thermoelectric materials for energy harvesting. *Adv. Energy Mater.* **5**, 1500588. doi: 10.1002/aenm.201500588 (2015).
8. Sales, B. C., Mandrus, D. & Williams, R. K. Filled skutterudite antimonides: A new class of thermoelectric materials. *Science* **272**, 1325–1328 (1996).
9. Siemens, M. E. *et al.* Quasi-ballistic thermal transport from nanoscale interfaces observed using ultrafast coherent soft X-ray beams. *Nature Mater.* **9**, 26–30 (2010).
10. Hu, Y. *et al.* Spectral mapping of thermal conductivity through nanoscale ballistic transport. *Nature Nanotech.* **10**, 701–706 (2015).
11. Zhao, W. Y. *et al.* Enhanced thermoelectric performance via randomly arranged nanopores: Excellent transport properties of $YbZn_2Sb_2$ nanoporous materials. *Acta Mater.* **60**, 1741–1746 (2012).
12. Liu, H. L. *et al.* Copper ion liquid-like thermoelectric. *Nature Mater.* **11**, 422–425 (2012).
13. Delaire, O. *et al.* Giant anharmonic phonon scattering in PbTe. *Nature Mater.* **10**, 614–619 (2011).
14. Pei, Y. Z. *et al.* Convergence of electronic bands for high performance bulk thermoelectric. *Nature* **473**, 66–69 (2011).
15. Liu, W. *et al.* Convergence of conduction bands as a means of enhancing thermoelectric performance of *n*-type $Mg_2Si_{1-x}Sn_x$ solid solutions. *Phys. Rev. Lett.* **108**, 166601 (2012).
16. Zhao, L. D. *et al.* Ultrahigh power factor and thermoelectric performance in hole-doped single-crystal SnSe. *Science* DOI: 10.1126/science.aad3749 (2015).
17. Rhyee, J. S. *et al.* Peierls distortion as a route to high thermoelectric performance in In_4Se_3-delta crystals. *Nature* **459**, 965–968 (2009).
18. Luo, Y. *et al.* Enhancement of the thermoelectric performance of polycrystalline $In_4Se_{2.5}$ by copper intercalation and bromine substitution. *Adv. Energy Mater.* **4**, 1300599 (2014).
19. Heremans, J. P. *et al.* Enhancement of thermoelectric efficiency in PbTe by distortion of the electronic density of states. *Science* **321**, 554–557 (2008).
20. Zhou, J., Yang, R. G., Chen, G. & Dresselhaus, M. S. Optimal bandwidth for high efficiency thermoelectric. *Phys. Rev. Lett.* **107**, 226601 (2011).
21. Zhao, W. Y. *et al.* Multi-localization transport behaviour in bulk thermoelectric materials. *Nature Commun.* **6**, 6197 (2015).
22. Pappas, P. T. The original ampere force and Biot-Savart and Lorentz forces. *Il Nuovo Cimento B Series 11*. **76**, 189–197 (1983).
23. Nolas, G. S., Cohn, J. L. & Slack, G. A. Effect of partial void filling on the lattice thermal conductivity of skutterudites. *Phys. Rev. B* **58**, 164 (1998).
24. Meisner, G. P. *et al.* Structure and lattice thermal conductivity of fractionally filled skutterudites: solid solutions of fully filled and unfilled end members. *Phys. Rev. Lett.* **80**, 3551–3554 (1998).
25. Rogl, G. *et al.* High-pressure torsion, a new processing route for thermoelectrics of high *ZT*s by means of severe plastic deformation. *Acta Mater.* **60**, 2146–2157 (2012).
26. Kim, H. *et al.* Structural order-disorder transitions and phonon conductivity of partially filled skutterudites. *Phys. Rev. Lett.* **105**, 265901 (2010).
27. Pei, Y. Z. *et al.* Improving thermoelectric performance of caged compounds through light-element filling. *Appl. Phys. Lett.* **95**, 042101 (2009).
28. Qiu, Y. T. *et al.* Charge-compensated compound defects in Ga-containing thermoelectric skutterudites. *Adv. Funct. Mater.* **23**, 3194–3203 (2013).
29. Li, H., Tang, X. F., Zhang, Q. J., & Uher, C. High performance $In_xCe_yCo_4Sb_{12}$ thermoelectric materials with in situ forming nanostructured InSb phase, *Appl. Phys. Lett.* 94, 102114(2009).
30. Shi, X. *et al.* Multiple-filled skutterudites: high thermoelectric figure of merit through separately optimizing electrical and thermal transports. *J. Am. Chem. Soc.* **133**, 7837–7846 (2011).
31. Zhao, W. Y. *et al.* Enhanced thermoelectric performance in barium and indium double-filled skutterudite bulk materials via orbital hybridization induced by indium filler. *J. Am. Chem. Soc.* **131**, 3713–3720 (2009).
32. Ravinder, D., Shalini, P., Mahesh, P. & Boyanov, B. S. High temperature thermoelectric power studies of cobalt and titanium substituted barium hexagonal ferrites. *J. Magn. Magn. Mater.* **268**, 154–158 (2004).
33. Nolas, G. S., Kendziora, C. A. & Takizawa, H. Polarized Raman-scattering study of Ge and Sn-filled $CoSb_3$. *J. Appl. Phys.* **94**, 7440–7443 (2003).

34. Caillat, T., Borshchevsky, A. & Fleurial, J. P. Properties of single crystalline semiconducting CoSb$_3$. *J. Appl. Phys.* **80**, 4442 (1996)
35. Pei, Y. Z. *et al.* Stabilizing the optimal carrier concentration for high thermoelectric efficiency. *Adv. Mater.* **23**, 5674–5678 (2011).
36. Kajikawa, Y. Analysis of high-temperature thermoelectric properties of p-type CoSb$_3$ within a two-valence-band and two-conduction-band model. *J. Appl. Phys.* **115**, 203716 (2014).
37. Julian, C. L. Theory of heat conduction in rare-gas crystals, *Phys. Rev.* **137**, A128–A137 (1965).
38. Dho, J., Lee, E. K., Park, J. Y. & Hur, N. H. Effects of the grain boundary on the coercivity of barium ferrite BaFe$_{12}$O$_{19}$. *J. Magn. Magn. Mater.* **285**, 164–168 (2005).
39. Chen, L. D. *et al.* Anomalous barium filling fraction and *n*-type thermoelectric performance of Ba$_y$Co$_4$Sb$_{12}$. *J. Appl. Phys.* **90**, 1864–1868 (2001).
40. Fonda, E. *et al.* Negative differential magnetization for Ni nanoparticels in Al. *Phys. Rev. B* **71**, 184411 (2005).
41. Costache, M. V., Bridoux, G., Neumann, I. & Valenzuela, S. O. Magnon-drag thermopile. *Nature Mater.* **11**, 199–202 (2012).
42. Grannemann, G. N. & Berger, L. Magnon-drag Peltier effect in a Ni-Cu alloy. *Phys. Rev. B* **13**, 2072–2079 (1976).
43. Morin, F. J. & Maita, J. P. Conductivity and Hall effect in the intrinsic range of germanium. *Phys. Rev.* **94**, 1525–1529 (1954).

Acknowledgements

This work was supported by the National Basic Research Program of China (973-program) No. 2013CB632505, National Natural Science Foundation of China (Nos. 11274248, 51521001, 51572210). XRD, DSC, FESEM, HRTEM and EPMA experiments were performed at Center for Materials Research and Testing of Wuhan University of Technology. Hall measurements were performed at State Key Lab of Advanced Technology for Materials Synthesis and Processing of Wuhan University of Technology. X-ray photoemission spectra were recorded at Key Laboratory of Catalysis and Materials Science of the State Ethnic Affair Commission & Ministry of Education of South-Central University for Nationalities. The measurements of static magnetic properties and low-temperature α were performed at School of Physics and Technology of Wuhan University. The Curie temperature was measured at Institute of Physics, CAS. Authors thank to S. B. Mu, W. Y. Chen, M. J. Yang, X. L. Nie, C. H. Shen, X. Q. Liu, and Y. Y. Qi for their help in the structure characterization, thank to K. Jin, X. L. Dong, J. Yuan, and Y. L. Huang for their help in measuring the Curie temperature of BaM-NPs, thank to S. Q. Xia and X. Y. Zhou for their help in the high temperature Hall measurements, and also thank to H. J. Liu for their valuable discussions on the role of BaM-NPs in adjusting TE properties.

Author Contributions

W. Z. and Q. Z. designed a magnetic nanocomposite thermoelectric material for this work. Z. L. synthesized the samples. Z. L., X. S., X. T., Y. C., S. L., and Y. P. carried out the thermoelectric properties and Hall measurements. Z. L. W. Z., and Y. L. performed the electron microscopy analysis and XPS experiments. W. Z., P. W. and J. S. performed the magnetic measurements. W. Z., Z. L., Q. Z. and J. Y. conceived the experiments, analyzed the results and wrote and co-wrote the manuscript. All authors discussed the results and commented on the manuscript.

Additional information

The authors declare no competing financial interests. Readers are welcome to comment on the online version of the paper. Supplementary information is available in the online version of the paper. Reprints and permission information is available online at www.nature.com/reprints. Correspondence and requests for materials should be addressed to Q.-J. Z. (zhangqj@whut.edu.cn) and J.-H. Y. (jihuiy@u.washington.edu).

Figure captions

Figure 1. Effect of BaM-NPs on microstructures. (**a**) FESEM photograph of Ba$_{0.3}$In$_{0.3}$Co$_4$Sb$_{12}$ matrix, (**b**) FESEM photograph and (**c**) HRTEM image of MNC45 magnetic nanocomposite TE material.

Figure 2. Hall measurement data in the temperature range of 300-775 K. Temperature dependences of (**a**) Hall coefficient, (**b**) carrier concentration and (**c**) mobility of$x$BaFe$_{12}$O$_{19}$/Ba$_{0.3}$In$_{0.3}$Co$_4$Sb$_{12}$.

Figure 3. Electrical and thermal transport properties in the range of 300-850 K. Temperature dependence of (**a**) electric conductivity, (**b**) Seebeck coefficient, (**c**) thermal conductivity, (**d**) carrier thermal conductivity, (**e**) lattice thermal conductivity, and (**f**) ZT of xBaM/Ba$_{0.3}$In$_{0.3}$Co$_4$Sb$_{12}$. The inset in (**b**) shows the temperature dependence of power factor.

Figure 4 Curie temperature of BaM-NPs. Temperature dependences of magnetization of BaM-NPs under the magnetic fields of 0.6 T and 2.0 T in the range of 300-800 K. The inset shows that the T_C of BaM-NPs is about 669 K under 0.6 T and about 673 K under 2.0 T.

Figure 5. Electrical transport properties before and after magnetization. Temperature dependence of (**a,c**) electric conductivity and (**b,d**) Seebeck coefficient of MNC00 and MNC35 before and after magnetization. It is showed the temperature dependences of σ and α of MNC00 and MNC35 before and after magnetization along the A, B and C direction for 24 hours under an applied magnetic field of 0.2 T. The curves were shifted upwards or downwards in order to clearly observe the evolutions of the σ and α induced by the magnetization.

Methods

Synthesis. The preparation process of xBaM/Ba$_{0.3}$In$_{0.3}$Co$_4$Sb$_{12}$ magnetic nanocomposite TE materials was given as follows: Firstly, highly pure metals Co, Sb, Ba and In were used to prepare Ba$_{0.3}$In$_{0.3}$Co$_4$Sb$_{12}$ matrix, and the detailed process was reported in elsewhere[44]. Secondly, micron-sized BaM powders had been ball-milled for 24 h and deposited in water to obtain BaM-NPs by discarding the coarse particles. The doping content of BaM-NPs was calculated according to x=0, 0.15%, 0.25%, 0.35% and 0.45%. Thirdly, BaM-NPs and the matrix were loaded into a beaker with alcohol solvent, then ultrasonically dispersed and mixed to form nanocomposite powders. Finally, the as-prepared nanocomposite powders were sintered into dense pellets by the spark plasma sintering (SPS) (SPS-1050 Dr Sinter) method at 923 K and 50 MPa. To reveal the effects of magnetoelectric interaction on the transport properties $_2$, after having measured the data of Figure 3, the samples MNC00 and MNC35 were first magnetized for 24 h (Figure S8) under an applied magnetic field of about 0.2T along the A direction and measured to obtain the σ and α, and then repeated the magnetization and measurement process along the B and C directions, respectively.

Characterization. The constituent phases were determined by powder X-ray diffraction (XRD) (PANalyticalX'Pert PRO) by using Cu $K\alpha$ radiation (λ=0.15418 nm). The chemical compositions were quantitatively analyzed with electron probe microanalysis (EPMA) (JEOL, JXA-8230). The microstructures were characterized with secondary electron image (SEI) of field emission scanning electron microscope (FESEM) (ULTRA, Plus-43-13). HRTEM images were investigated with field emission transmission electron microscope (TEM) JEM-2100F). To investigate the effect of BaM-NPs on the electron structure of the matrix, X-ray photoelectron spectra (XPS) of Sb 3$d_{5/2}$

and $3d_{3/2}$ core levels were recorded at pass energy of 25 eV, step size of 0.05 eV and 128 scans with Thermo VG Multilab 2000 spectrometer. To investigate the effect of BaM-NPs on the crystal structure of the matrix, Raman-scattering measurements were carried out by using a microscopic confocal laser Raman spectrometer (RENISHAW- INVIA).

Transport measurement. The σ and α were measured with the standard four-probe method (Sinkuriko, ZEM-3) in the range of 300-850 K. The κ was calculated by using the equation $\kappa=\lambda\rho_0 C_p$, where C_p is the specific heat capacity, ρ is the bulk density, and λ is the thermal diffusivity coefficient. λ was measured in the range of 300-850 K with laser flash technique (Netzsch, LFA-427). C_p was measured by using a TA Q2000 differential scanning calorimeter. ρ_0 was obtained by Archimedes method (Sartorius, YDK01). The κ_E was calculated by the Wiedemann-Franz law as $\kappa_E=L\sigma T$ (L is Lorenz number and $L=2.0\times10^{-8}$ V^2K^{-2})[45]. κ_L was obtained by using the equation $\kappa_L=\kappa-\kappa_E$. Uncertainties of σ and κ are ± 5-7%. Uncertainty of α is ± 5%. Hall coefficient (R_H) and electrical resistivity (ρ) in the range of 300-775 K were measured by Van der Pauw method under a reversible magnetic field of 1.5 T. The carrier concentration (n) and Hall mobility (μ_H) were calculated by using the formula $n=1/(R_H e)$ and $\mu_H=R_H/\rho$, respectively. To investigate the magnon-drag thermopower induced by BaM-NPs, the α of un-magnetized MNC00 and MNC35 in the range of 90-300 K were were measured under zero field and a magnetic field of 0.4 T with a PPMS-9 (Quantum Design INC., USA). To confirm the existence of the magnetic transition from ferromagnetism to paramagnetism in xBaM/$Ba_{0.3}In_{0.3}Co_4Sb_{12}$ in the intrinsic excitation region, the T_C of BaM-NPs was determined by the temperature dependences of magnetization of BaM-NPs in the range of 300-800 K that were measured with a PPMS-9 (Quantum Design INC., USA) under a magnetic field of 0.6 T and 2.0 T, respectively. To ensure whether xBaM/$Ba_{0.3}In_{0.3}Co_4Sb_{12}$ is magnetic TE materials, the magnetization versus magnetic field of BaM-NPs, MNC00, and MNC45 were measured with a PPMS-9 (Quantum Design INC., USA) at room temperature.

References for the Methods

44. Zhao, W. Y. *et al.* Synthesis and high temperature transport properties of barium and indium double-filled skutterudites $Ba_xIn_yCo_4Sb_{12-z}$. *J. Appl. Phys.* **102**, 113708 (2007).
45. Dyck, J. S. *et al.* Thermoelectric properties of the *n*-type filled skutterudite $Ba_{0.3}Co_4Sb_{12}$ doped with Ni. *J. Appl. Phys.* **91**, 3698–3705 (2002).

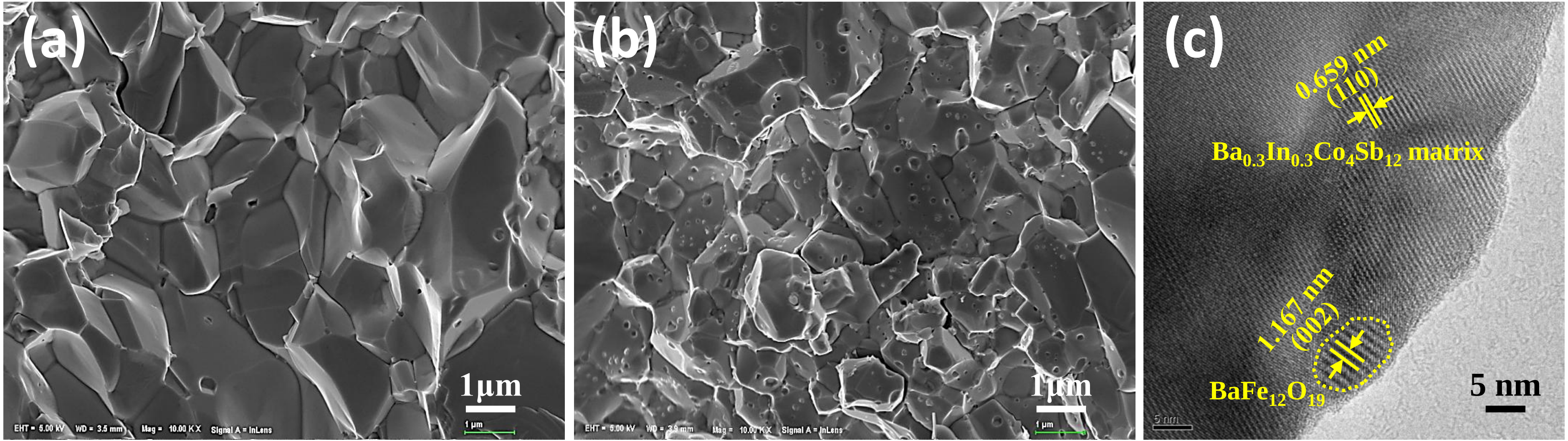
(a)
1μm
EHT = 5.00 kV WD = 3.5 mm Mag = 10.00 K X Signal A = InLens
1 μm
(b)
1μm
EHT = 5.00 kV WD = 3.9 mm Mag = 10.00 K X Signal A = InLens
1 μm
(c)
0.659 nm
(110)
$Ba_{0.3}In_{0.3}Co_4Sb_{12}$ matrix
1.167 nm
(002)
$BaFe_{12}O_{19}$
5 nm
5 nm

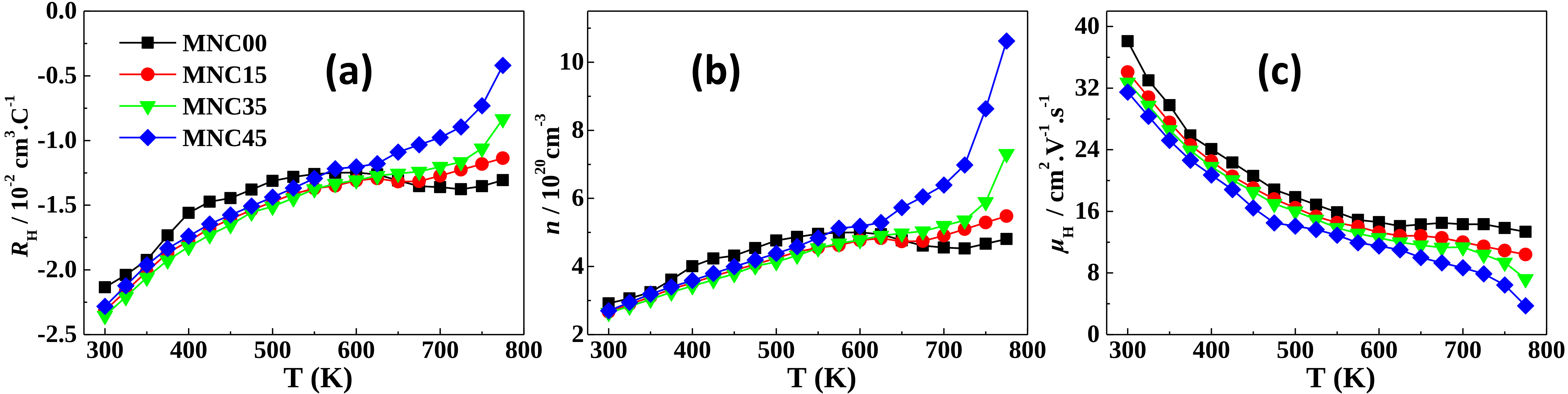
(a)
(b)
(c)
MNC00
MNC15
MNC35
MNC45
R_H / 10^{-2} cm^3.C^{-1}
n / 10^{20} cm^{-3}
μ_H / cm^2.V^{-1}.s^{-1}
T (K)
0.0
-0.5
-1.0
-1.5
-2.0
-2.5
2
4
6
8
10
0
8
16
24
32
40
300
400
500
600
700
800

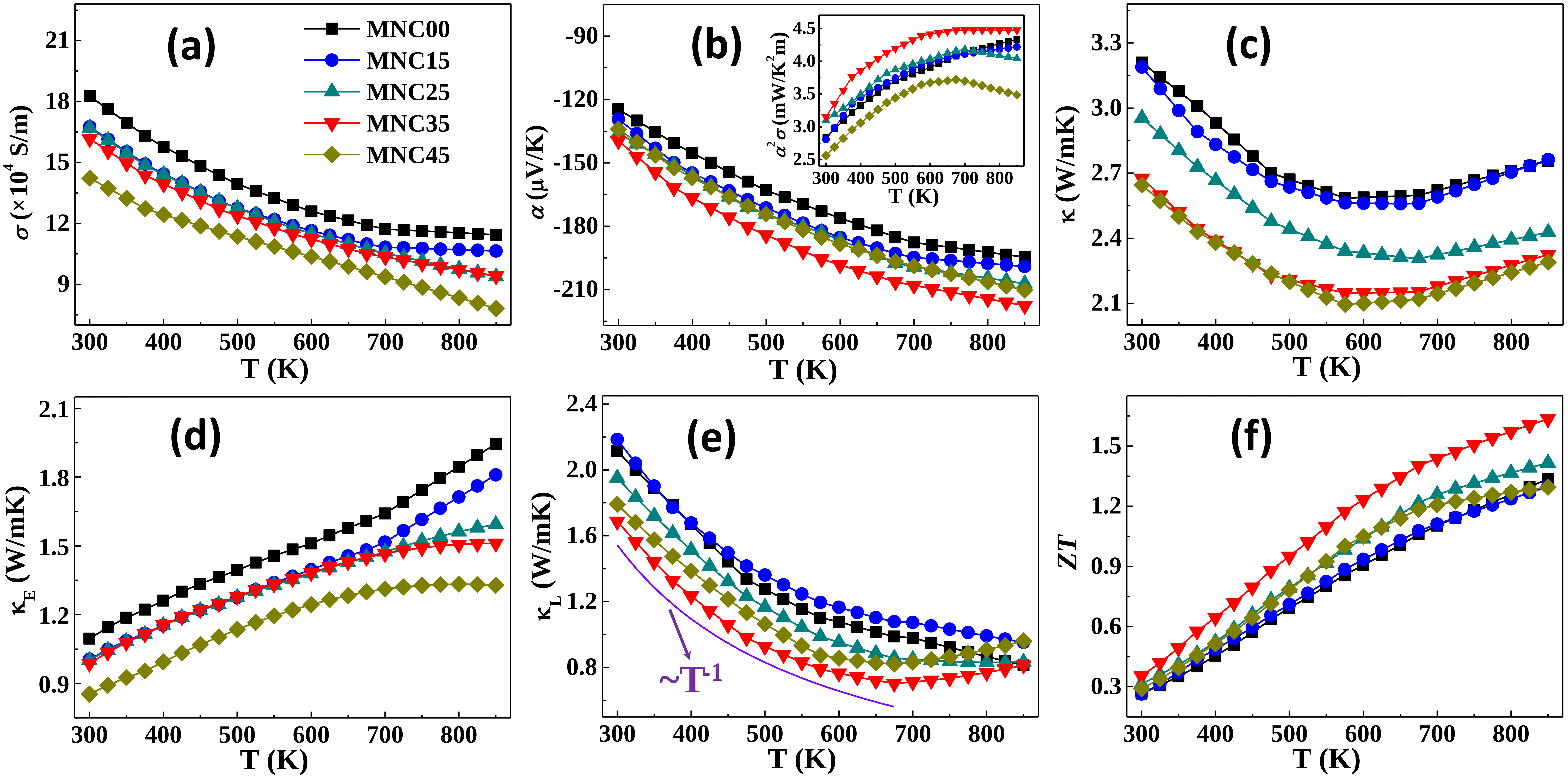
(a)
MNC00
MNC15
MNC25
MNC35
MNC45
σ (×10^4 S/m)
21
18
15
12
9
300
400
500
600
700
800
T (K)
(b)
α (μV/K)
-90
-120
-150
-180
-210
α²σ (mW/K²m)
4.5
4.0
3.5
3.0
2.5
300 400 500 600 700 800
T (K)
300
400
500
600
700
800
T (K)
(c)
κ (W/mK)
3.3
3.0
2.7
2.4
2.1
300
400
500
600
700
800
T (K)
(d)
κ_E (W/mK)
2.1
1.8
1.5
1.2
0.9
300
400
500
600
700
800
T (K)
(e)
κ_L (W/mK)
2.4
2.0
1.6
1.2
0.8
~T^-1
300
400
500
600
700
800
T (K)
(f)
ZT
1.5
1.2
0.9
0.6
0.3
300
400
500
600
700
800
T (K)

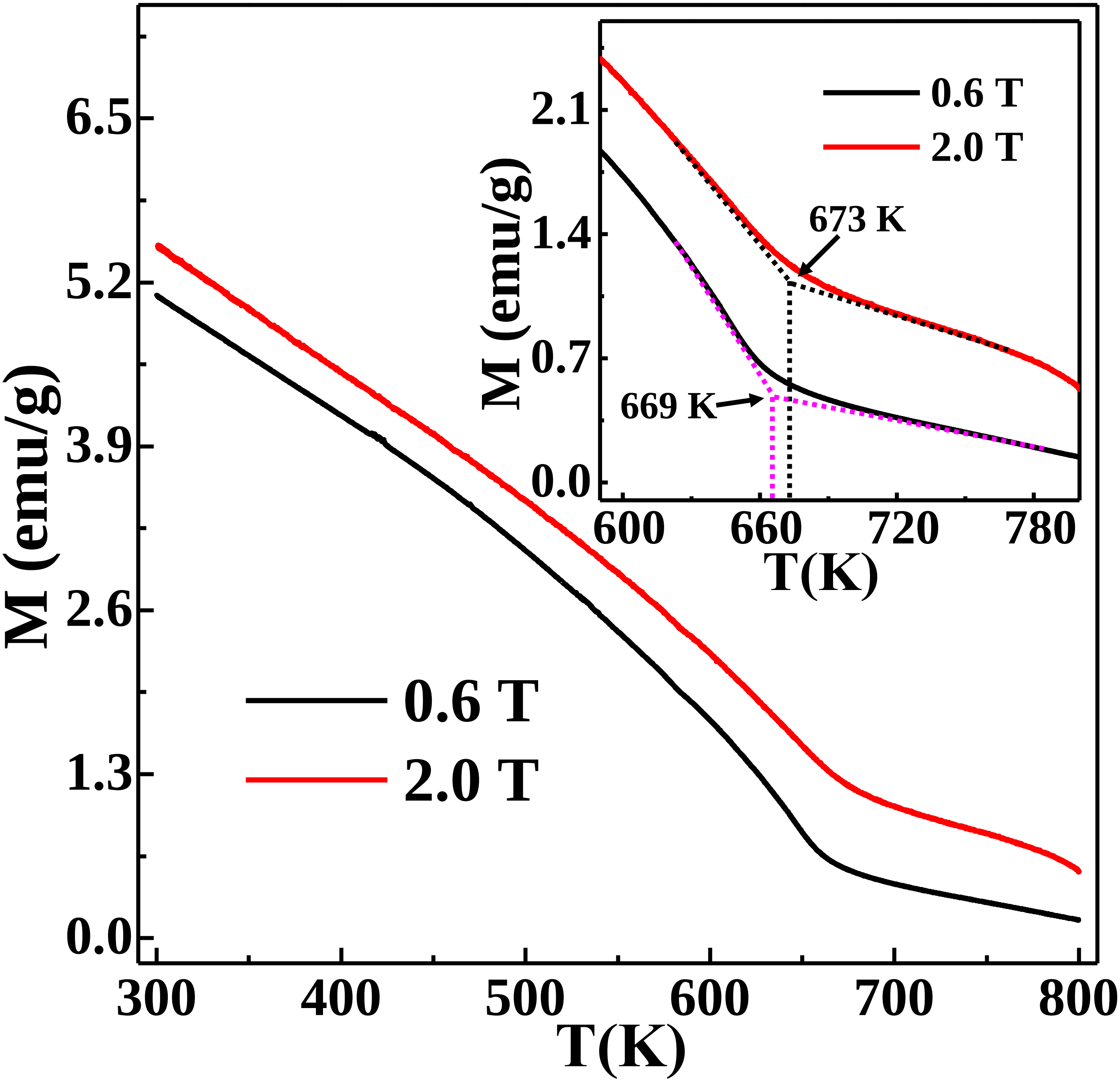
M (emu/g)
T(K)
0.0
1.3
2.6
3.9
5.2
6.5
300
400
500
600
700
800
0.6 T
2.0 T
M (emu/g)
T(K)
0.0
0.7
1.4
2.1
600
660
720
780
0.6 T
2.0 T
673 K
669 K

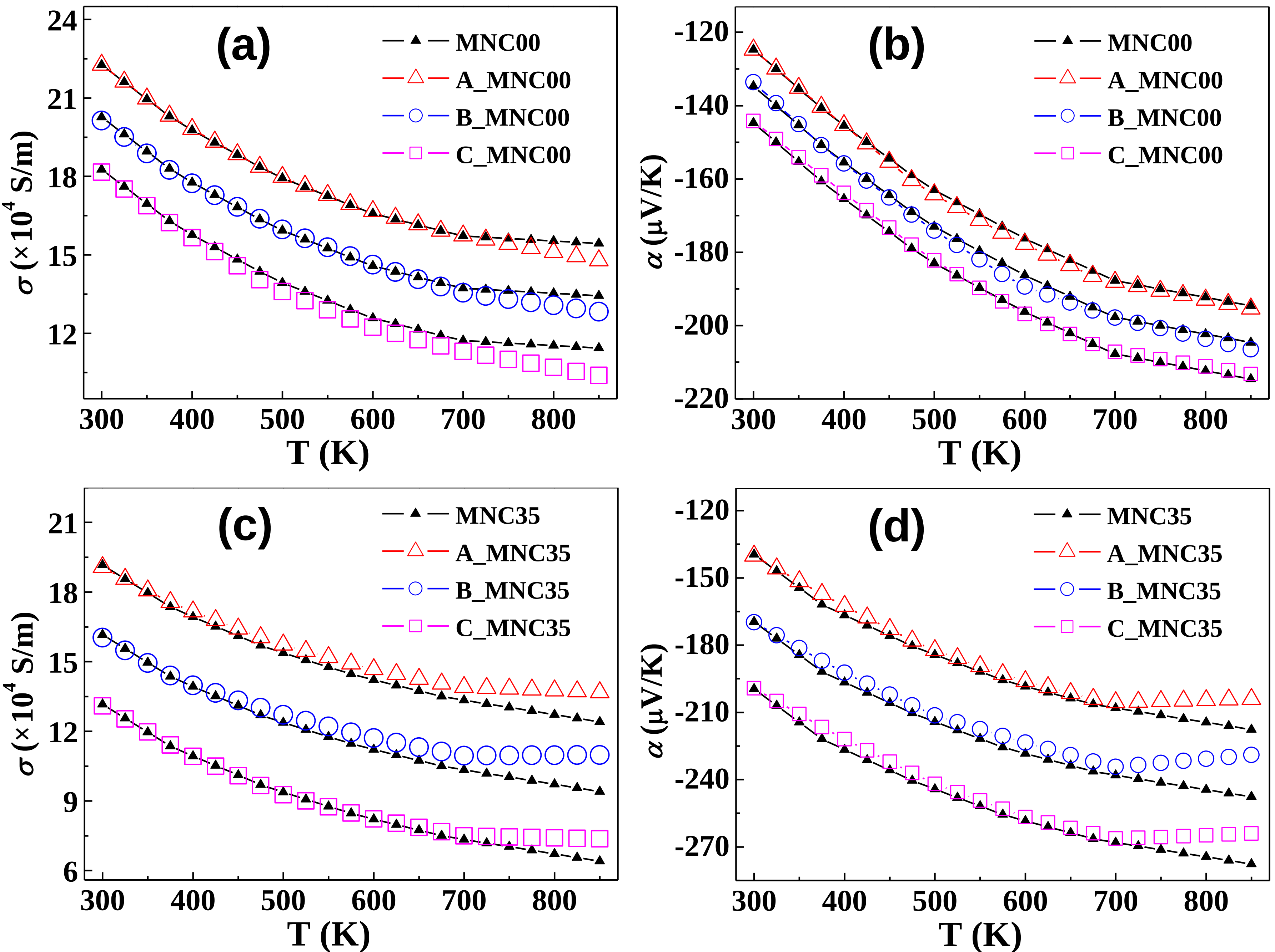
(a)
σ (×10⁴ S/m)
24
21
18
15
12
300
400
500
600
700
800
T (K)
MNC00
A_MNC00
B_MNC00
C_MNC00
(b)
α (μV/K)
-120
-140
-160
-180
-200
-220
300
400
500
600
700
800
T (K)
MNC00
A_MNC00
B_MNC00
C_MNC00
(c)
σ (×10⁴ S/m)
21
18
15
12
9
6
300
400
500
600
700
800
T (K)
MNC35
A_MNC35
B_MNC35
C_MNC35
(d)
α (μV/K)
-120
-150
-180
-210
-240
-270
300
400
500
600
700
800
T (K)
MNC35
A_MNC35
B_MNC35
C_MNC35